of the carbohydrate ring. A similar stereochemistry is not available for the mannoside. Clearly, more studies on this aspect of complex formation are required. Low-intensity ^{51}V NMR signals were also observed at -506 and -514 ppm in the mannoside system. Because of the line widths of the various signals, no effort was made to quantitatively assess the spectra.

Conclusions

The hydroxyl groups of six-membered cyclic molecules such as pyranosides and 1,2-cyclohexanediols form acyclic vanadate esters and cyclic complexes analogous to those observed earlier with ethylene glycol.[13] However, the geometric constraints imposed by the cyclic ligands strongly influence the equilibrium constants for formation of the various complexes and are probably responsible for the formation of some types of complexes not previously observed with ligands containing only hydroxyl groups. Esterification of axial hydroxyls by vanadate is disfavored, while formation of cyclic complexes is strongly favored for ligands with cis compared to those with trans vicinal hydroxyl groups. Although cyclic complexes were not detected with methyl β-D-glucopyranoside, such a complex was observed to form with methyl α-D-glucopyranoside, however, with a formation constant about 60 times smaller than that for the analogous complex with methyl β-D-galactopyranoside. This observation is in keeping with the occurrence of ring flattening associated with the replacement of a carbon of the cyclohexane ring by an oxygen. Ring flattening increases the dihedral angle between the adjacent diequatorial C-O bonds of the trans hydroxyls from the nominal 60° of the unperturbed system. The corresponding angles between the hydroxyls in the cis arrangement are decreased from 60°. The smaller angle favors formations of a five-membered cyclic product. On this basis, it is expected that cyclic products formed from the methyl glucosides will be less favored than those from the methyl galactosides and mannosides, and this is observed.

A complex, binuclear in vanadium, but with mixed-coordination structure is formed with the methyl D-galactosides, but there is no evidence for such a complex with methyl α-D-mannopyranoside, possibly because the vicinal *cis*-hydroxyls of the galactosides are sufficiently close to the 6-hydroxyl group for some interaction that is not possible with the mannoside.

It is apparent from these studies that both the types and the stabilities of the vanadate complexes formed from these ligands are very sensitive to subtle changes in ligand structure.

The formation of 5-coordinate vanadate complexes with the vicinal hydroxyls of six-membered cyclic molecules may be relevant to possible effects of vanadate on the metabolism of inositol phosphates and phosphatidyl inositol,[18,19] which is thought to involve, in some cases, the formation of an inositol 1,2-cyclic phosphate.[20] The pentacoordinate uridine vanadate complex presumably inhibits the function of ribonuclease because the complex resembles the transition state for formation and hydrolysis of the uridine 2',3'-cyclic phosphate intermediate of the enzymatic reaction. Analogous behavior might be expected for enzymes that catalyze formation or hydrolysis of inositol cyclic phosphates.

Acknowledgment. Thanks are gratefully extended to the Natural Sciences and Engineering Research Council of Canada (M.J.G.), the Medical Research Council of Canada (M.J.G.), and the British Columbia Heart Foundation (A.S.T.) for their financial support of this work.

Contribution from the Department de Quimica Inorganica and Department de Fisica, Universitat de Barcelona, 08028 Barcelona, Spain, and Department of Chemistry, North Carolina State University, Raleigh, North Carolina 27695-8204

Importance of Metal-Metal Interactions through the P-P Bonds for the Multidimensional Electrical Properties of MP_4 (M = V, Cr, Mo)

Santiago Alvarez,*[1a] Josep Fontcuberta,*[1b] and Myung-Hwan Whangbo*[1c]

Received January 22, 1988

The electronic structures of MP_4 (M = V, Cr, Mo) were examined by performing tight-binding band calculations on VP_4. The MP_4 phase has a structure in which metal atom chains are sandwiched between P_4^{2-} layers. Despite this apparently one-dimensional character, the t_{2g}-block bands of VP_4 are dispersive not only along the chain but also along the interchain and interlayer directions. Our study shows that the multidimensional nature of those bands originates from the fact that metal atom chains interact with one another through the P-P bonds of the P_4^{2-} layers. Our Fermi surface calculations reveal that VP_4 is a three-dimensional metal, while CrP_4 and MoP_4 are semimetals.

In the past two decades, the series of transition-metal phosphides MP_4 (M = V; M = Cr, Mo, W; M = Mn, Tc, Re; M = Fe, Ru, Os) have been obtained.[2] The first member of the series, VP_4, contains one-dimensional chains of metal atoms parallel to the *c* axis[3] and shows metallic conductivity. The same structure is found for CrP_4 and MoP_4, both of which exhibit metallic properties.[4a] WP_4 is observed to be a poor metal, but its exact structure has not been determined yet.[4b] MnP_4, TcP_4, and ReP_4 do not form chains of metal atoms but consist of metal-metal dimers.[5-8] Three different structural modifications exist for MnP_4, all of which are semiconductors and differ in the way the Mn_2 dimers are connected to one another. FeP_4, RuP_4, and OsP_4 have structures with no metal-metal bonds,[9-11] and all of them are diamagnetic semiconductors. MP_4 phases for M = Ti, Co, Ni, and Cu have not been made, whereas non-transition-metal MP_4 phases are known (e.g., CdP_4,[12] MgP_4,[13] and $MgAs_4$[14]).

---

(1) (a) Departament de Quimica Inorganica, Universitat de Barcelona. (b) Departament de Fisica, Universitat de Barcelona. (c) North Carolina State University.

(2) For a recent review, see: Jeitschko, W.; Florke, M.; Moller, M.-H.; Ruhl, R. *Ann. Chim. Fr.* **1982**, *7*, 525.

(3) Jeitschko, W.; Florke, M.; Scholz, M. D. *J. Solid State Chem.* **1984**, *52*, 320.

(4) (a) Jeitschko, W.; Donohue, P. C. *Acta Crystallogr., Sect. B: Struct. Crystallogr. Cryst. Chem.* **1972**, *B28*, 1893. (b) Kinomura, N.; Terao, K.; Kikkawa, S.; Koizumi, M. *J. Solid State Chem.* **1983**, *48*, 306.

(5) Jeitschko, W.; Donohue, P. C. *Acta Crystallogr., Sect. B: Struct. Crystallogr. Cryst. Chem.* **1975**, *B31*, 574.

(6) Ruhl, R.; Jeitschko, W. *Acta Crystallogr., Sect. B: Struct. Crystallogr. Cryst. Chem.* **1981**, *B37*, 39.

(7) Ruhl, R.; Jeitschko, W.; Schwochau, K. *J. Solid State Chem.* **1982**, *44*, 134.

(8) Jeitschko, W. Ruhl, R. *Acta Crystallogr., Sect. B: Struct. Crystallogr. Cryst. Chem.* **1979**, *B35*, 1953.

(9) (a) Jeitschko, W.; Braun, D. J. *Acta Crystallogr., Sect B: Struct. Crystallogr. Cryst. Chem.* **1978**, *B34*, 3196. (b) Sugitani, M.; Kinomura, M.; Koizumi, M.; Kume, S. *J. Solid State Chem.* **1978**, *26*, 195. (c) Grandjean, F.; Gerard, A.; Kriger, M.; Heiden, C.; Braun, D. J.; Jeitschko, W. *Solid State Commun.* **1980**, *33*, 261.

(10) (a) Evain, M.; Broc, R.; Fiechter, S.; Tributsh, H. *J. Solid State Chem.* **1987**, *71*, 40. (b) Fiechter, S.; Tributsch, H.; Evain, M.; Brec, R. *Mater. Res. Bull.* **1987**, *22*, 543.

(11) (a) Braun, D. J.; Jeitschko, W. *Z. Anorg. Allg. Chem.* **1978**, *445*, 157. (b) Florke, M.; Jeitschko, W. *J. Less-Common Met.* **1982**, *86*, 247.

(12) Krebs, H.; Muller, K.-H.; Zurn, G. *Z. Anorg. Allg. Chem.* **1956**, *285*, 15.

(13) (a) Gibinski, T.; Cisowaska, E.; Zdanowivz, W.; Henkie, Z.; Wojakowski, A. *Krist. Tech.* **1974**, *9*, 161. (b) El Maslout, A.; Zanne, M.; Jeannot, F.; Gleitzer, Ch. *J. Solid State Chem.* **1975**, *14*, 85. (c) von Schnering, H. G.; Menge, G. *Z. Anorg. Allg. Chem.* **1976**, *422*, 219.

0020-1669/88/1327-2702$01.50/0

Despite its apparently one-dimensional (1D) structural character, VP_4 does not exhibit any electronic instability such as a charge density wave (CDW) phenomenon, thereby suggesting the presence of strong interchain interactions in VP_4.[15] To understand this apparently puzzling problem, we examine the band electronic structure of VP_4. In the following, we first describe the crystal structure of VP_4 and discuss the t_{2g}-block bands of VP_4 and its associated Fermi surfaces. Then the qualitative features of these d-block bands are analyzed and the structural factors responsible for the multidimensional electrical properties of VP_4 are discussed.

Crystal Structure of VP_4

In order to understand the band electronic structure of VP_4, which determines its electrical and magnetic properties, it is necessary first to examine its crystal structure. Shown in **1** is a hypothetical P_4 layer formed by fusing P_6 rings with boat conformations. This structure differs from that of black phosphorus,[16,17] in which the P_6 rings have a chair conformation. Shown in **2** is the P_4^{2-} layer that results from the P_4 layer **1** by adding two electrons and therefore breaking one P–P bond per formula unit P_4. It is the P_4^{2-} layer **2** that is found in VP_4, CrP_4, and MoP_4. Note that the P_4^{2-} layer consists of P_{10} rings and has two kinds of phosphorus atoms (i.e., P^0 and P^-). The P^0 atoms bear one lone pair, but the P^- atoms bear two lone pairs. Therefore, toward a transition-metal ion, the P^0 and P^- atoms can act as two- and four-electron donors, respectively. In MP_4 (M = V, Cr, Mo), the M^{2+} cations are sandwiched between the P_4^{2-} layers, so that layers of the M^{2+} cations and the P_4^{2-} layers alternate along the *b* axis.

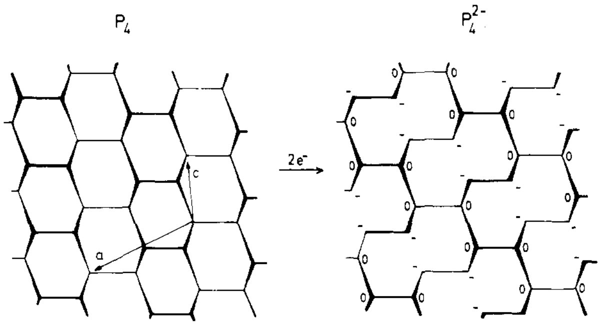

1 2

Let us now examine the occurrence of the metal chains and the coordination environment of each metal ion in MP_4 (M = V, Cr, Mo), in terms of the schematic diagram **3**. Shown in **3** is how the M^{2+} cations are placed above and below a P_4^{2-} layer, where they form chains parallel to the *c* axis. The metal ions above the layer are shown by filled circles. The large and small filled circles represent the metal ions bonded to four and two phosphorus atoms of the layer lying below, respectively. The metal ions below the P_4^{2-} layer are represented by empty circles. The large and small empty circles represent the metal ions bonded to two and four phosphorus atoms of the layer lying above, respectively. The metal ions of **3** lying above or below the P_4^{2-} layer complete their octahedral coordination by bonding to the phosphorus atoms of another P_4^{2-} layer that sandwiches them. The metal ions bonded to four (two) phosphorus atoms of the bottom P_4^{2-} layer require two (four) phosphorus atoms of the upper P_4^{2-} layer to complete their octahedral coordination. Thus, with respect to the bottom P_4^{2-} layer, the upper P_4^{2-} layer is shifted along the *c* axis.

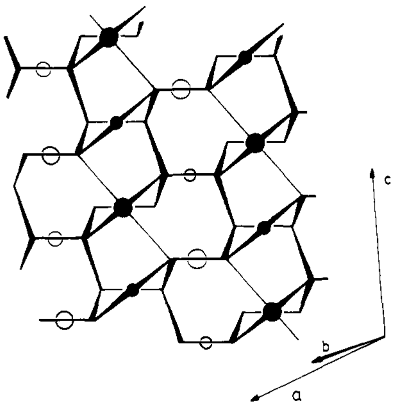

3

As a result of sandwiching with two P_4^{2-} layers, each metal ion is coordinated by two P^- and two P^0 atoms from the one P_4^{2-} layer and by two P^- atoms of the other P_4^{2-} layer as schematically shown in **4** for a single metal ion chain. As expected, the P^0 and P^- atoms coordinate one and two metal atoms, respectively. Clearly, all the metal ions equivalent, but they do not have the same height along the *b* axis so that they form a zigzag chain.

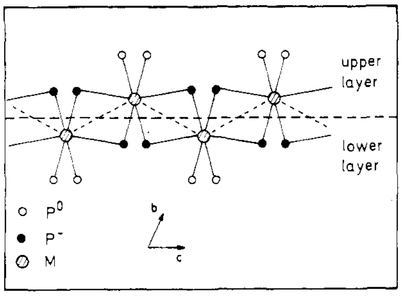

4

Depicted in **5** is a schematic diagram that shows how the metal chains are sandwiched by the P_4^{2-} layers, where the shaded circles represent the metal atom chains viewed along the *c* axis. There are two metal atoms per unit along the chain direction so that the primitive unit cell of VP_4, which is triclinic, contains two formula units, $(VP_4)_2$.

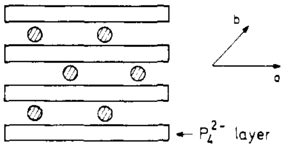

5

It is convenient to consider each metal chain of the MP_4 phase (M = V, Cr, Mo) as if it is constructed from MP_6 octahedra by sharing their edges. Shown in **6a** is a perspective view of an M_2P_{10} unit that results from two MP_6 octahedra by sharing an edge. The M_2P_{10} dimer unit can also be represented by the projection view **6b**. When the M_2P_{10} dimer units share their edges as indicated in **7**, we obtain the M_2P_8 chains that are present in the MP_4 phase.

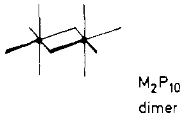

6a

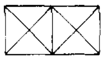

6b

Band Electronic Structure

In the present section we examine the electronic structure of VP_4 by performing tight-binding band calculations[18] based upon the extended Hückel method.[19] The atomic parameters employed

---

(14) Gerardin, R.; Aubry, J.; Courtois, A.; Protas, J. *Acta Crystallogr., Sect. B: Struct. Crystallogr. Cryst. Chem.* **1977**, *B33*, 2091.

(15) DiSalvo, F. J.; Waszczak, J. V. *Mater. Res. Bull.* **1985**, *20*, 351.

(16) Brown, A.; Rundquist, S. *Acta Crystallogr.* **1965**, *19*, 684.

(17) Burdett, J. K.; McLarnan, T. *J. Chem. Phys.* **1981**, *75*, 5764.

(18) (a) Whangbo, M.-H.; Hoffmann, R. *J. Am. Chem. Soc.* **1978**, *100*, 6093. (b) Whangbo, M.-H.; Hoffmann, R.; Woodward, R. B. *Proc. R. Soc. London* **1979**, *A366*, 23.

(19) Hoffmann, R. *J. Chem. Phys.* **1963**, *39*, 1397.

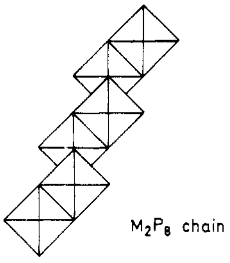

7

in our study are summarized in Table I. Since the Fermi level of MP_4 (M = V, Cr, Mo) lies within its t_{2g}-block bands, we will consider only these bands in the following.

A. t_{2g}-Block Bands. Figure 1 shows the dispersion relations of the t_{2g}-block bands (i.e., those bands derived primarily from the metal t_{2g}-block levels) of VP_4 calculated along the $\Gamma \rightarrow X$, $\Gamma \rightarrow Y$, and $\Gamma \rightarrow Z$ directions. Since a unit cell consists of two formula units, $(VP_4)_2$, there are six t_{2g}-block bands. Note that these bands are dispersive not only along the chain direction $\Gamma \rightarrow Z$ but also along the interchain direction $\Gamma \rightarrow X$ and the interlayer direction $\Gamma \rightarrow Y$. With the formal oxidation state of V^{2+}, there are six electrons per unit cell to fill the t_{2g}-block bands. As shown in Figure 1, the Fermi level for VP_4 cuts the lower three t_{2g}-block bands in nearly all directions. Therefore, it is predicted that VP_4 is not a 1D but a three-dimensional (3D) metal, which is consistent with the observation[15] that VP_4 does not exhibit a CDW phenomenon despite the presence of seemingly isolated metal atom chains. The density of states (DOS) of VP_4 calculated for the energy region of the t_{2g}-block bands is shown in Figure 2. The DOS value peaks in the lower energy region of the t_{2g}-block bands, since the bottom three bands are less dispersive than the upper three (see Figure 1).

CrP_4 is isostructural with VP_4 and is believed to be semimetallic.[4] Within the rigid band scheme, the band structure of CrP_4 may be simulated by Figure 1 upon adding eight d electrons to the t_{2g}-block bands. The Fermi level relevant for CrP_4 cuts the upper three t_{2g}-block bands in all three directions. Thus, CrP_4 is expected to be a 3D metal. Figure 2 shows that the Fermi level for CrP_4 occurs near the lowest point of the DOS valley centered around −9 eV. Thus, CrP_4 might be a semimetal, as suggested on the basis of its electrical conductivity as a function of temperature.[4]

Also indicated in Figures 1 and 2 are the Fermi levels appropriate for MnP_4 and TiP_4 under the assumption that they have the VP_4 structure. Clearly, for MnP_4, the band levels with strongly metal–metal antibonding character are filled, which is energetically unfavorable. It is of interest to note that all known phases of MnP_4 (i.e., 2-MnP_4, 6-MnP_4, and 8-MnP_4)[5,6] do not have the VP_4 structure but a "broken-chain" structure. So far TiP_4 has not been made, but it might have interesting metallic properties if it has the VP_4 structure.

B. Fermi Surfaces. Figure 3 shows cross sections of the four Fermi surfaces calculated for VP_4. Figure 3a,b depicts 3D hole pockets centered around Γ, and Figure 3c shows a tunnellike hole aligned along the $\Gamma \rightarrow Z$ direction. Figure 3d reveals a cross-section view of the electron Fermi surface in which "electron tunnels" run along the $A \rightarrow R$ and $B \rightarrow R$ directions. Here $A = (0.5a^*, 0, 0.5c^*)$, $B = (0, 0.5b^*, 0.5c^*)$, and $R = (0.5a^*, 0.5b^*, 0.5c^*)$. The two-dimensional nature of the Fermi surface of Figure 3c suggests that the electrical conductivity of VP_4 would be smaller along the chain than along the interchain or interlayer direction. It would be interesting to measure the resistivity anisotropy of VP_4.

Figure 4 shows the 3D hole and electron pockets calculated for CrP_4 on the basis of the VP_4 band structures. The hole pocket, centered at Γ, has a dimension $\sim 0.5c^* \times 0.2a^* \times 0.2b^*$. The electron pocket, centered at $\sim(0.45a^*, 0.25b^*, 0.15c^*)$, has the dimension $\sim 0.2a^* \times 0.15c^* \times 0.3b^*$. Figure 4 clearly shows CrP_4 to be a semimetal. Since MoP_4 is isostructural and isoelectronic with CrP_4, MoP_4 is also expected to be a semimetal.

Table I. Atomic Parameters

atom	orbital	H_{ii}, eV	ζ_1	ζ_2	C_1[a]	C_2[a]
V	4s	−8.81	1.60			
	4p	−5.52	1.60			
	3d	−11.00	4.75	1.50	0.4558	0.7516
P	3s	−18.60	1.60			
	3p	−14.00	1.60			

[a] Contraction coefficients used in the double-ζ expansion.

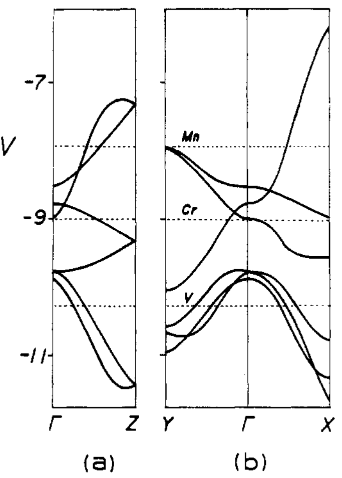

Figure 1. Dispersion relations of the t_{2g}-block bands calculated for VP_4: (a) along the chain direction; (b) along the interchain and the interlayer directions. In units of the reciprocal vectors a^*, b^*, and c^*, $\Gamma = (0, 0, 0)$, $X = (a^*/2, 0, 0)$, $Y = 0, b^*/2, 0)$, and $Z = (0, 0, c^*/2)$. The dashed lines with the symbols V, Cr, and Mn refer to the Fermi levels appropriate for VP_4, CrP_4, and MnP_4 within a rigid band approximation.

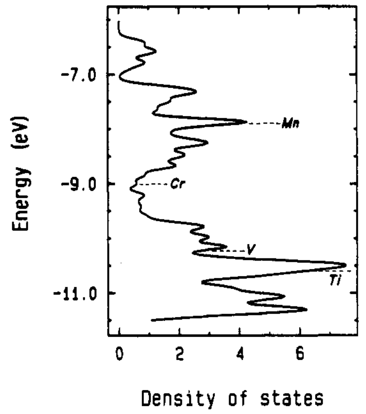

Figure 2. Density of states calculated for VP_4 in the energy region of the t_{2g}-block bands. The Fermi levels calculated for TiP_4, VP_4, CrP_4, and MnP_4, within a rigid band approximation, are also indicated.

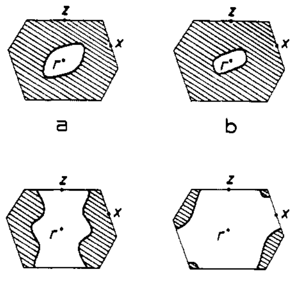

Figure 3. Cross sections of the four Fermi surfaces calculated for VP_4. The hole pockets in (a) and (b) are centered at Γ, the tunnellike "hole" in (c) runs along the $\Gamma \rightarrow Z$ direction, and the electron tunnels in (d) run along the $A \rightarrow R$ and $B \rightarrow R$ directions. Here $A = (0.5a^*, 0, 0.5c^*)$, $B = (0, 0.5b^*, 0.5c^*)$, and $R = (0.5a^*, 0.5b^*, 0.5c^*)$.

Orbital Interactions

As shown in the previous section, the t_{2g}-block bands of VP_4 are dispersive not only along the chain $\Gamma \rightarrow Z$ but also along the

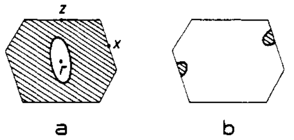

Figure 4. Fermi surfaces of CrP_4 calculated on the basis of the VP_4 band structure: (a) cross section of the hole pocket centered at Γ; (b) projection of the electron pocket centered at ($0.45a^*$, $0.25b^*$, $0.15c^*$) on the $\overline{X\Gamma Z}$ plane. For simplicity, the equivalent electron pocket centered at ($-0.45a^*$, $-0.25b^*$, $-0.15c^*$) is not shown.

interchain (Γ→X) and the interlayer (Γ→Y) directions. We now examine how this multidimensional character of the t_{2g}-block bands is brought about on the basis of orbital interactions and the crystal structure. In the following, we first examine the t_{2g}-block bands of the V_2P_8 chain **7** and then discuss the structural origin of why these bands are dispersive along the interchain and interlayer directions.

A. t_{2g}-Block Bands of the V_2P_8 Chain. To emphasize the octahedral environment of each vanadium atom, the V_2P_8 chain **7** may be represented by **8**. An ideal V_2P_8 chain may be obtained from regular VP_6 octahedra with the V–P distance of 2.40 Å (i.e., the average V–P distance of VP_4),[3] which leads to the V–V distance of 3.39 Å. The real V_2P_8 chain found in VP_4 consists of distorted VP_6 octahedra, in which the V–V distance is 3.24 Å.[3] In our study, the real V_2P_8 chain was simulated by bending the V–P–V angles of the ideal V_2P_8 chain (from 90 to 84°) so as to obtain the V–V distance of 3.24 Å. Figure 5a shows the t_{2g}-block bands of the resulting V_2P_8 chain, which are similar in nature to the t_{2g}-block bands of VP_4 along the Γ→Z direction.

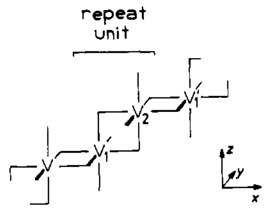

8

9

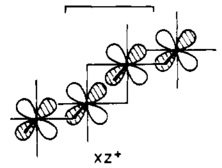

10

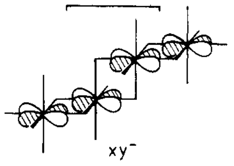

11

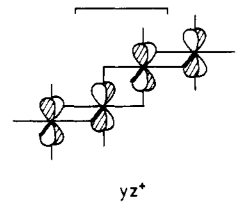

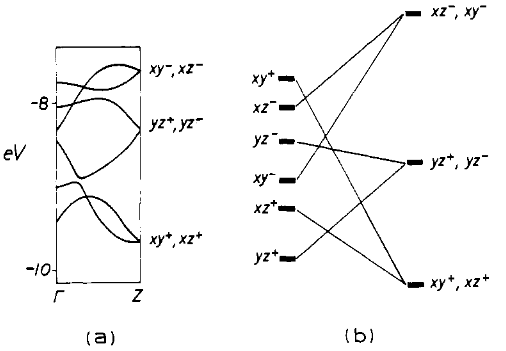

Figure 5. Electronic structure of the V_2P_8 chain: (a) t_{2g}-block band structure; (b) qualitative energy levels of the t_{2g}-block levels of the V_2P_8 chain at Γ and Z.

Table II. Bonding Characteristics of the t_{2g} Crystal Orbital of the V_2P_8 Chain

orbital	intracell	intercell (Γ point)	intercell (Z point)
xy^+	π	σ^*	σ
xy^-	π^*	σ	σ^*
xz^+	σ	π	π
xz^-	σ^*	π	π^*
yz^+	π	π	π
yz^-	π^*	π^*	π

As indicated in Figure 5a, the t_{2g}-block bands of the V_2P_8 chain are composed of the in-phase (+) and out-of-phase (−) combinations of the metal d_{xy}, d_{xz}, and d_{yz} orbitals. For example, the xz^+, xy^-, and yz^+ band orbitals at Γ are represented by **9**, **10**, and **11**, respectively. The band orbitals can be classified according to their nodal properties (σ, π, or δ) and interaction nature (bonding or antibonding) both within a unit cell and between nearest-neighbor unit cells. Thus, for example, the xz^+ orbital (**9**) is σ-bonding within a unit cell but π-antibonding between nearest-neighbor unit cells. The xy^- orbital (**10**) is π-antibonding within a unit cell but σ-bonding between nearest-neighbor unit cells. The yz^+ orbital (**11**) is π-bonding both within a unit cell and between nearest-neighbor unit cells. The characteristics of the six t_{2g} band orbitals at Γ and Z are summarized in Table II, which helps us understand the essential features of the t_{2g}-block bands VP_4 in Figure 5a. Since σ-interactions are typically stronger than π-interactions, the sum of the intra- and intercell interactions would increase in strength in the order

$$(\sigma, \pi) < (\sigma, \pi^*), (\pi, \pi) < (\pi, \pi^*) < (\sigma^*, \pi), (\pi^*, \pi^*) < (\sigma^*, \pi^*) \quad (1)$$

On the basis of the above sequence, the six bands level at Γ are correlated with those at Z, as shown in Figure 5b. The t_{2g}-block bands of the V_2P_8 chain (Figure 5a) agree well with those predicted from Figure 5b after allowing for symmetry-imposed avoided crossings. Note that the dispersion patterns of Figure 5a are similar to those of Figure 1a along the Γ→Z direction. The middle band of Figure 1a is represented by yz orbitals, and metal–metal π-type interactions are responsible for its dispersion. The upper and lower bands of Figure 1a are more dispersive than the middle band due to their xy orbitals, which provide metal–metal σ-type interactions between unit cells (see **10** and Table II).

B. Interchain and Interlayer Interactions. Figure 1 shows that band dispersion is substantial either along the interchain direction (Γ→X) or along the interlayer direction (Γ→Y). Such interchain and interlayer interactions are responsible for the multidimensional electrical properties of VP_4. To understand the structural origin of this aspect, we examine the crystal structure of **3** in some detail.

Metal atoms of VP_4 are linked along the a and b directions (i.e., interchain and interlayer directions, respectively) through the P–P units of the P_4^{2-} layers. It is the sp^3 orbital (i.e., n_σ in **12a**) of the P^0 atom and the p and sp^2 orbitals (i.e., n_p and n'_σ in **12b** and **12c**, respectively) of the P^- atom that provide the through-bond interactions of metal atoms via the P–P bonds. Along the a

12a

12b

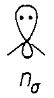

12c

direction, metal atoms are linked by the P^0–P^0 and P^-–P^- linkages as shown in **13a** and **13b**, respectively. The P–P bonds around the P^0–P^0 and P^-–P^- linkages have gauche arrangements as indicated by the Newman projections **14b** and **14a**, respectively.

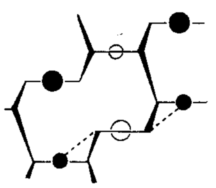

13a

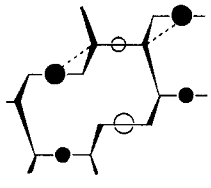

13b

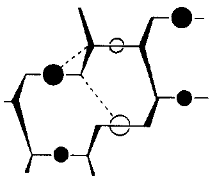

13c

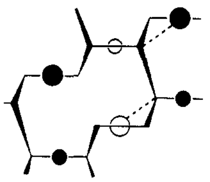

13d

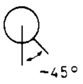

14a

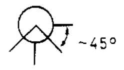

14b

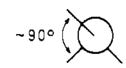

14c

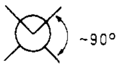

14d

Along the *b* and $(b - c/2)$ directions, metal atoms interact across the P_4^{2-} layers through the P^0–P^- and P^0–P^0 bridges as shown in **13c** and **13d**, respectively. The P–P bonds around the P^0–P^- linkage of **13c** have a gauche arrangement (**14c**), while those around the P^0–P^0 linkage of **13d** have a trans arrangement (**14d**).

In **14d** two n_σ orbitals on the P^0 centers are trans to each other, so the in-phase and out-of-phase combinations of these orbitals (n_+ and n_-, respectively, shown in **15**) effectively couple metal atoms across the P_4^{2-} layers. In **14a–c** the n_σ, n_p, or n'_σ orbitals of the two phosphorus centers do not have a trans arrangement. Nevertheless, the gauche arrangement allows the n_σ, n_p, or n'_σ orbitals to form n_+- and n_--like combinations. Since such orbitals contain π-like orbital components across the P–P linkages, they allow the metal t_{2g}-block levels to effectively interact through the P–P linkages.

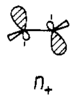

15a

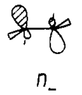

15b

Concluding Remarks

The present study shows that the t_{2g}-block bands of VP_4 are dispersive both along the chain direction and along the interchain and interlayer directions. This multidimensional character of the t_{2g}-block bands originates from the fact that the metal atom chains of VP_4 interact through the P–P bonds of the P_4^{2-} layers. Our Fermi surface calculations suggest that the electrical conductivity of VP_4 would be smaller along the chain than along the interchain or interlayer direction. Within a rigid band approximation, our study suggests that CrP_4 and MoP_4 are semimetals, in agreement with the available experimental data. Provided that TiP_4 is made to have the VP_4 structure, it would be metallic with a high density of states at the Fermi level.

Acknowledgment. Work at North Carolina State University was in part supported by the U.S. Division of Materials Sciences, Office of Basic Energy Sciences, U.S. Department of Energy, under Grant DE-FG05-86ER45259. Work at the Universitat de Barcelona was supported by the Direction General de Investigacion Cientifica y Tecnia through Grant PB86-0272. We express our appreciation for computing time made available by DOE on the ER-Cray X-MP computer. We thank Dr. Michel Evain for his help with Fermi surface calculations and plotting.

Contribution from the Institut für Anorganische Chemie
der Universität Hannover, D-3000 Hannover, FRG

Infrared Spectra of Matrix-Isolated $CF_3S(O)F$ and Its Photolysis Product CF_3OSF

Dietmar Bielefeldt, Gabriele Schatte, and Helge Willner*

Received January 8, 1988

By UV photolysis of matrix-isolated trifluoromethanesulfinyl fluoride, $CF_3S(O)F$, the isomer CF_3OSF is formed. Structural and bonding parameters of this first fluorosulfenyl ester are evaluated from the vibrational frequencies of the natural and the ^{13}C- and ^{18}O-enriched species. CF_3OSF is decomposed by prolonged UV irradiation to COF_2 and SF_2. Attempts to photoisomerize $CF_3S(O)F$ on a preparative scale lead to mixtures of COF_2, SOF_2, CF_3SSCF_3, and C_2F_6 in the gas phase as well as in solution.

Introduction

Sulfoxylic acid, H_2SO_2, and some of its derivatives are very unstable and therefore rarely characterized.[1] The following chart classifies the derivatives of sulfoxylic acid into stable and unstable species:

	SCl_2	$ClSOH$	$S(OH)_2$	$HOSF$	SF_2
stable		$ClSOR$	$S(OR)_2$	$ROSF$	unstable
		$ClSNR_2$	$S(NR_2)_2$	R_2NSF	

R = organic substituent

Of the unstable species, only SF_2 has been synthesized[2] and fully characterized.[3] The fluorosulfenyl esters CH_3OSF and C_2H_5OSF had been postulated[4] as products of the reaction of $(CH_3O)_2S$ with SSF_2. A reinvestigation by the same authors, however, showed that the ^{19}F NMR signals of CH_3F and C_2H_5F had been misassigned to the fluorosulfenyl esters.[5] Thus, no

---

(1) Houben-Weyl-Müller. *Methoden der organischen Chemie*: *Organische Schwefelverbindungen*: Büchel, K. H., et al., Eds.; Thieme: Stuttgart, FRG, 1985; Vol. E11.

(2) Deroche, J. C.; Bürger, H.; Schulz, P.; Willner, H. *J. Mol. Spectrosc.* **1981**, *89*, 269.

(3) Gombler, W.; Haas, A.; Willner, H. *Z. Anorg. Allg. Chem.* **1980**, *469*, 135.

(4) Seel, F.; Budenz, R.; Gombler, W. *Z. Naturforsch., B: Anorg. Chem., Org. Chem., Biochem., Biophys., Biol.* **1970**, *25B*, 885.

(5) Seel, F.; Gombler, W.; Budenz, R. *Z. Naturforsch., B: Anorg. Chem., Org. Chem., Biochem., Biophys., Biol.* **1972**, *27B*, 78.

0020-1669/88/1327-2706$01.50/0